DATA ACQUISITION AND PROCESSING PLATFORM DESIGN FOR SHINE WIRE SCANNER

J. Dong*, J. Chen, S. S. Cao, F. Z. Chen, L. Y. Yu, R. X. Yuan

SSRF, Shanghai, China

INTRODUCTION

- Motivated by the successful operation of X-ray FEL facilities worldwide and the great breakthroughs in atomic, molecular, and optical physics, condensed matter physics, matter in extreme conditions, chemistry and biology, the first hard X-ray FEL light source in China, the Shanghai HIgh repetition rate XFEL aNd Extreme light facility (SHINE) is under construction. The SHINE will utilize a photocathode electron gun combined with the superconducting Linac to produce 8 GeV FEL quality electron beams with 1 MHz repetition rate.
- Wire Scanner is widely used for beam profile measurements. A fork equipped with thin wires passes through the electron beam. The wire interaction with the beam produces scattered electrons and showered particles downstream the wire scanner unit which are detected by photomultipliers.
- At the SHINE, each wire scanner unit consists of two motorized forks (horizontal and vertical plane) driven by a linear servo motor. This 90° configuration of motors helps to avoid vibration influences. The Beam Loss Monitors (BLMs) downstream of the wire scanner motion units are used for detection of scattered particles.

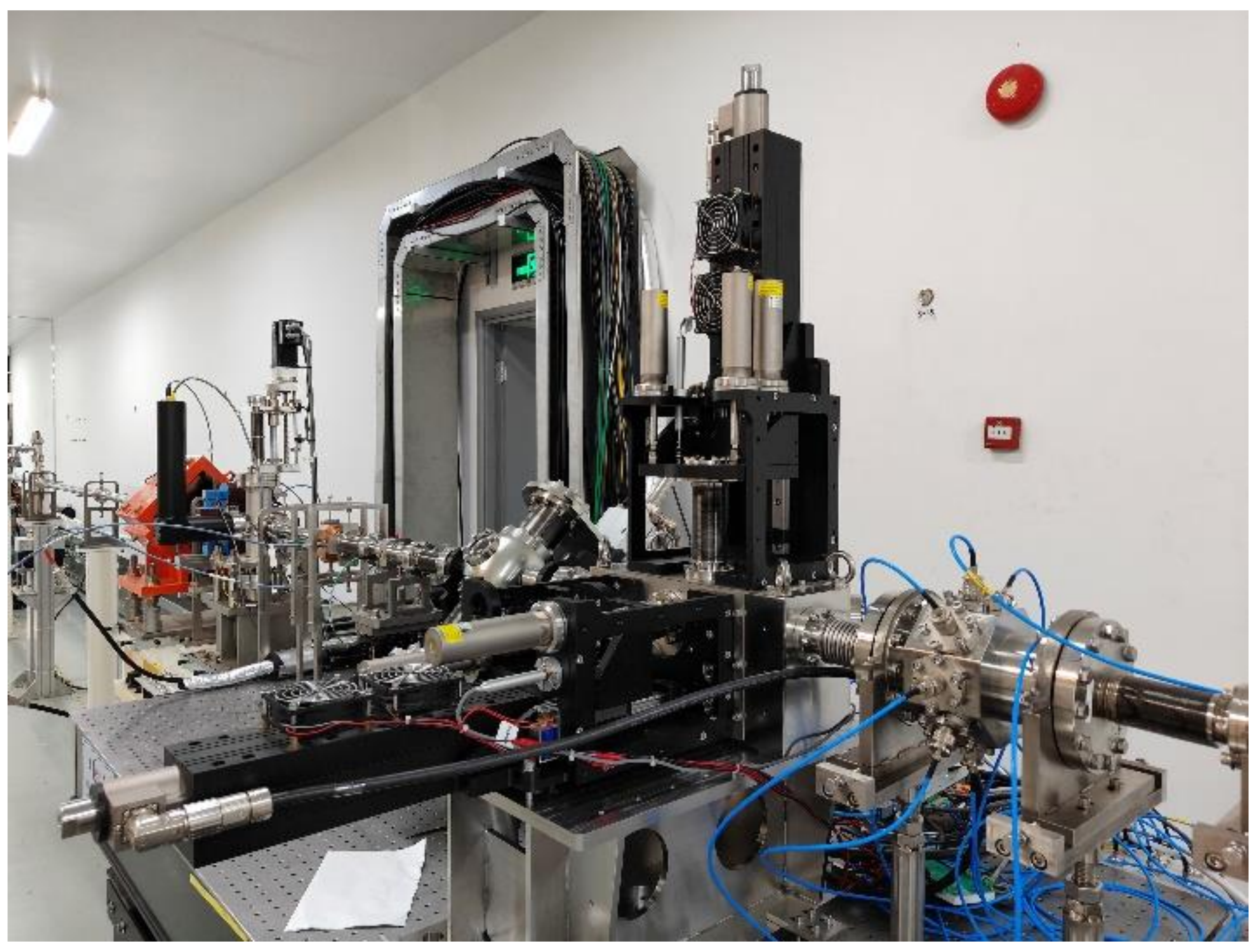

Figure 1: Wire scanner motion unit at the SXFEL

DATA ACQUISITION AND PROCESSING SYSTEM

- The PMTs and preamplifiers, which convert the BLM Cherenkov light pulse and LED heartbeat light pulse into a time-shaped voltage signal, are mounted on the signal conditioning board. The BLM and Beam Position Monitor (BPM) signals are digitized and processed with the system. The magnetic railings ruler is installed next to the linear motor track to measure the position of wires. The signal outputted by the magnetic railings ruler is collected and analyzed by the data acquisition board. The wire scan processing software calculates the beam parameters by merging the beam loss data, beam positions and the wires positions.
- Figure 2 shows the structural block diagram of the data acquisition system. The analog signal acquisition module digitalizes the input signals and provides the trigger and clock interfaces. The operational amplifiers are used to convert the four input signals from single-ended to differential. The amplitude of the input signal can also be adjusted by changing the gain to maximize the ADC dynamic range. The buffers are used for external trigger signals and user-defined signals to improve their driving capabilities. The performance of operational amplifiers in the ADC front-end analog circuits directly affects the performance of the system. The fully differential amplifiers LMH5401 is selected.

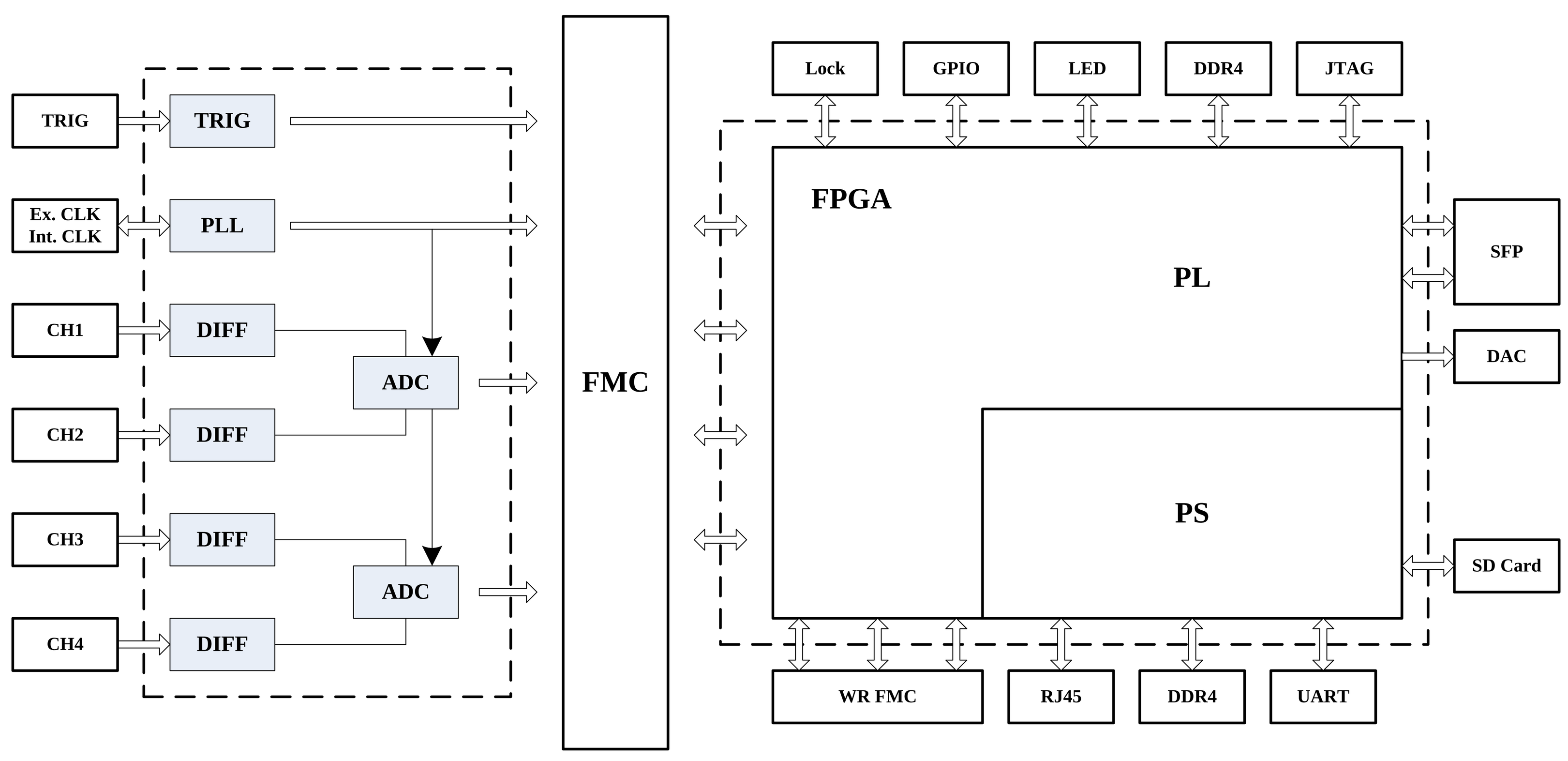

Figure 2: The structural block diagram of the data acquisition system. The carrier and mezzanine card design is adopted to meet the requirements of subsequent upgrades and updates.

- The quality of the sampling clock is one of the key factors determining the performance of the data acquisition system. The jitter of the sampling clock leads to the aperture error which affects the signal-to-noise ratio of the ADC and decreases the system performance. The clock of the ADC front-end analog circuits generated by the onboard crystal oscillator or external clock is used for the sampling clock, synchronization clock of ADC, and the FPGA high-speed serial transceiver. The HMC7044 is selected which is the industry's highest performance clock conditioner with JEDEC JESD204B support.
- The FPGA of the digital carrier board adopts the ZYNQ UltraScale+ MPSOC architecture which includes the Processing System (PS) and Programmable Logic (PL), and provides flexibility for complex multitasking designs. The digital motherboard contains a variety of interfaces, such as RJ45, GPIO, SFP+, etc. In order to meet the requirements of subsequent upgrades and updates, the FMC+ standard interface has been adopted to connect the ADC daughter board and the White Rabbit board.
- The beam profile density distribution is gaussian distribution. Therefore, the signal of wire scanner can be thought as superposition of three gaussian distributions. The three gaussian peaks from left to right represent the beam density distribution in vertical or horizontal directions individually. The signal strength can be expressed as Eq. 1. Using the detected signal data, an equation related to μ and Y(μ) could be established, then the vertical and horizontal beam profile sizes will be got by solving the equation with nonlinear least squares method.

$$Y(\mu) = Y_0 + A_1 e^{-\frac{(\mu-\mu_1)^2}{2\sigma_1^2}} + A_2 e^{-\frac{(\mu-\mu_2)^2}{2\sigma_2^2}} + A_3 e^{-\frac{(\mu-\mu_3)^2}{2\sigma_3^2}} \quad (1)$$

BEAM MEASUREMENTS AT THE SXFEL

- Beam size measurements have been performed using the wire scanner. The beam charge was ~500pC. Two wire scanner measurements were performed. The first measurement result is shown in Fig.3. The measured beam sizes have been compared with the measured beam sizes by the scintillating screens. The measurement results in the horizontal and vertical directions of the scintillating screens are 178μm and 98μm. There is a discrepancy in the beam size measured by the wire scanner and the screen. The beam size measured by the wire scanner is less than the size measured by the screen. The screen is affected by the thickness, angle, and the point spread function, causing the measured size to be larger than the wire scanner measured size. Therefore, the wire scanner measured beam sizes are more reliable than the screen. The second measurement result is shown in Fig. 4. The beam size was changed by the quadrupole magnets.

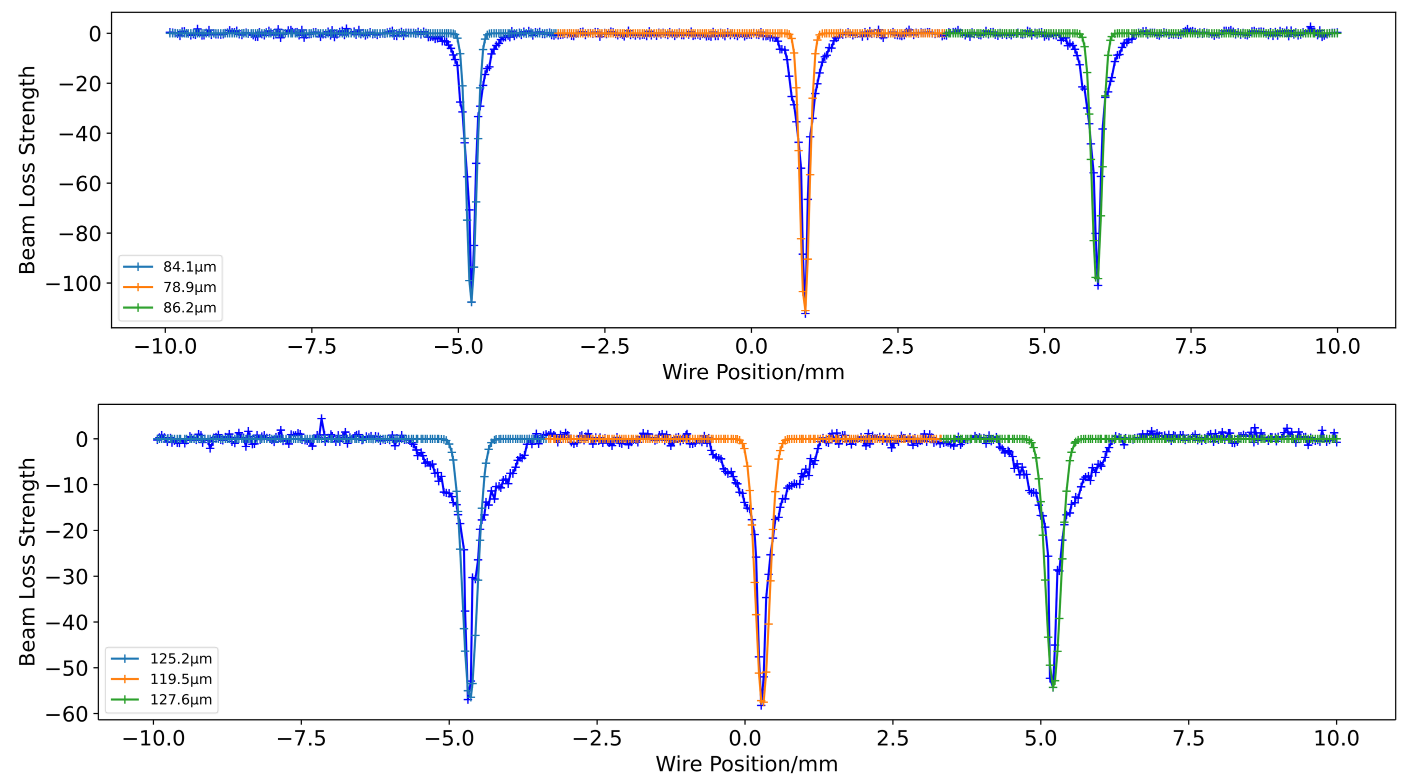

Figure 3: The first wire scanner measurement result at the SXFEL.

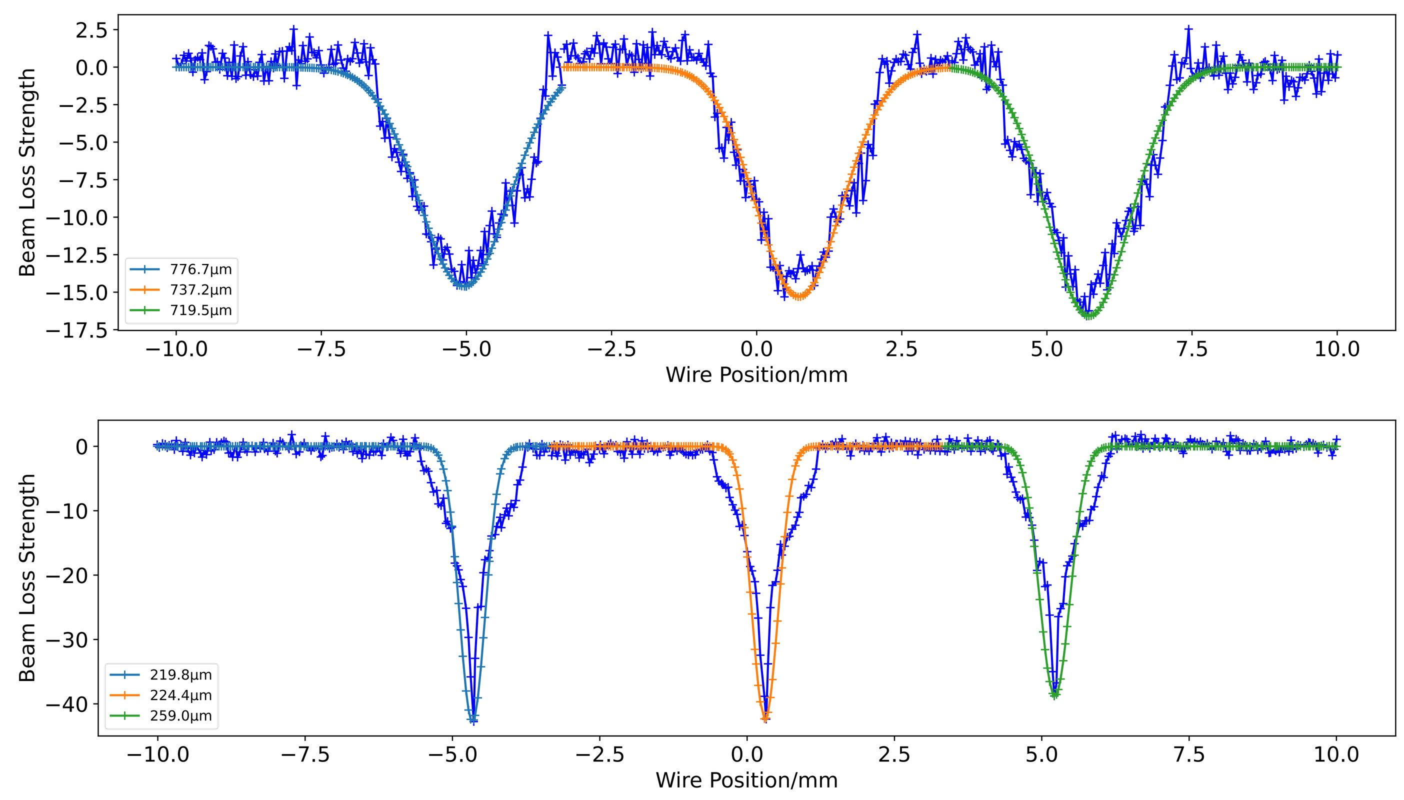

Figure 4: The second wire scanner measurement result at the SXFEL.

ACKNOWLEDGEMENTS

We would like to acknowledge the support of colleagues in the SSRF accelerator research center. Especially, thank for the help and cooperation from the operators of the SXFEL LINAC.

Contact: dongj@sari.ac.cn

(K. Li et al. 2018; T. Lensch et al. 2019; T. Lensch et al. 2018)

*Work supported by the NSFC (Grant No. 12105346)